Effect of surface stress on the stiffness of thin elastic plates and beams

Michael J. Lachut and John E. Sader*

Department of Mathematics and Statistics, The University of Melbourne, Victoria 3010, Australia

(Received 7 September 2011; revised manuscript received 23 January 2012; published 28 February 2012)

Nanomechanical doubly-clamped beams and cantilever plates are often used to sense a host of environmental effects, including biomolecular interations, mass measurements, and responses to chemical stimuli. Understanding the effects of surface stress on the stiffness of such nanoscale devices is essential for rigorous analysis of experimental data. Recently, we explored the effects of surface stress on cantilever plates and presented a theoretical framework valid for thin plate structures. Here, we generalize this framework and apply it to cantilever plates and doubly-clamped beams, exploring in detail the relative physical mechanisms causing a stiffness change in each case. Specifically, Poisson's ratio is found to exert a dramatically different effect in cantilevers than in doubly-clamped beams, and here we explain why. The relative change in effective spring constant is also examined, and its connection to the relative frequency shift is discussed. Interestingly, this differs from what is naively expected from elementary mechanics. Finally, a discussion of the practical implications of our theoretical findings is presented, which includes an assessment of available experimental results and potential future measurements on nanoscale devices.

DOI: 10.1103/PhysRevB.85.085440 PACS number(s): 68.37.Ps, 85.85.+j

I. INTRODUCTION

Mechanical devices such as microcantilever beams have emerged as a standard platform for a host of applications, including ultrasensitive mass measurements, biomolecular sensing, and detection of chemical analytes,[1–23] and has driven recent developments in nanoelectromechanical systems (NEMS).[5–24] Reduction in size, however, also enhances the influence of surface effects, which must be considered when interpreting measurements. In particular, knowledge of the effects of surface stress on device stiffness is essential for accurate mass measurements and has motivated a plethora of experimental and theoretical studies.[5–34] Surface stress can be routinely measured using the plate bending technique, which has been investigated theoretically in several studies.[35–38]

One approach to modeling the effects of surface stress on the stiffness of microcantilever beams, uses the so-called axial force model.[18–21,30–32] First proposed by Lagowski *et al.*,[21] this model assumes that application of strain-independent surface stress is equivalent to an axial force along its longitudinal axis. However, this model was subsequently shown to be unphysical by Gurtin *et al.*,[25] who concluded that within the framework of classical beam theory, strain-independent surface stress has no effect on cantilever beam stiffness. Even so, numerous reports have since used this unphysical axial force model and coincidentally show good agreement with measurements.[20,21,32]

Surface elasticity was also investigated by Gurtin *et al.*,[25] who proposed a general constitutive equation for surface stress.[39] Gurtin *et al.* showed that cantilever stiffness can indeed be affected by surface elasticity, but this effect is too small to explain the experimental results of Ref. 21. Subsequent theoretical investigations have also included surface elasticity, with similar conclusions.[26,29,30,33,34]

In a previous study,[27] we examined the effect of surface stress on a cantilever plate of arbitrary aspect ratio (length/width). Solution using a rigorous three-dimensional analysis revealed that strain-independent surface stress does indeed affect the stiffness of cantilever plates of finite aspect ratio. Importantly, this effect vanishes as the plate aspect ratio tends to infinity – consistent with Gurtin *et al.*[25] who implicitly considered this formal limit. Even so, the predicted effect is orders of magnitude smaller than experimental observations.[15,16,19–21,32] Experimental observations claiming that strain-independent surface stress affects the stiffness of cantilever beams thus remain unaccounted for theoretically.

The situation for doubly-clamped beams differs significantly. First, we note that the effect of in-plane stress, due to piezoelectric loading, on the stiffness of doubly-clamped beams has been studied rigorously.[40] This theoretical and experimental investigation established that the underlying mechanism is indeed due to an axial load along the axis of the doubly-clamped beam. However, the effect of surface stress on doubly-clamped beams has not been extensively investigated in comparison. We address this issue here and provide a detailed analysis of this loading case for doubly-clamped beams.

In this article, we expand and generalize the theoretical formalism of Ref. 27 and explore the physical mechanisms underlying the numerical results in that study. Specifically, we (i) present a general theoretical framework to calculate the effects of strain-independent surface stress on the stiffness of thin plates and beams, under arbitrary boundary conditions; (ii) examine application of this formalism to thin doubly-clamped beams and cantilever plates; (iii) present numerical results for the stress distribution and curvature which explains the coupling mechanism driving the change in cantilever stiffness due to surface stress; (iv) investigate the physical mechanism behind the observed Poisson's ratio dependence on the stiffness change in cantilever plates, which differs significantly to that of doubly-clamped beams; (v) explain the observed difference in the relative frequency shift and the relative stiffness change, for cantilever plates, which differs from the result naively expected from elementary mechanics; (vi) examine the relationship between the effective stiffness of doubly-clamped beams and cantilever plates, demonstrating that the former gives higher sensitivity to surface

stress, and (vii) present an expanded discussion of current and potential measurements in the context of the present theory.

We commence by reviewing the theoretical framework of Refs. 27 and 28, while summarizing all key assumptions. An analytical solution is obtained for doubly-clamped beams. Results for cantilever plates are then presented, together with a detailed discussion of the underlying physical mechanisms driving the observed change in stiffness – stress distributions and deflection functions are also presented. A comparison between doubly-clamped beams and cantilever plates follows, and we conclude with a discussion of the practical implications of the presented theory.

II. THEORY

In this section, we present a formal analysis of surface stress effects on the stiffness of thin doubly-clamped beams and cantilever plates. To examine the stiffness of both mechanical devices, two equivalent approaches can be used: (i) calculate the change in resonant frequency ω or (ii) the change in effective spring constant k_{eff}. The former case is most commonly reported in practice and was the preferred choice in our previous work.[27,28] Here, we explore both cases and discuss their relationship for thin doubly-clamped beams and cantilever plates.

We, first, consider the related problem of a completely unrestrained thin isotropic linearly elastic plate, with strain-independent surface stress applied to both faces, i.e., σ_s^+ and σ_s^- on upper and lower faces, respectively; see Fig. 1. Throughout this article, both σ_s^+ and σ_s^- are taken to be the changes in surface stress from their base (intrinsic) values.

We focus on the total surface stress defined by, $\sigma_s^T = \sigma_s^+ + \sigma_s^-$,[27,28,39,41] which is complimentary to the differential surface stress, $\Delta\sigma_s = \sigma_s^+ - \sigma_s^-$.[35,36,41] Within the framework of linear elasticity, bending does not affect the stiffness of a beam or plate. Since differential surface stress, $\Delta\sigma_s$, induces bending, it is ignored in the analysis that follows.[35,36,41]

Application of a uniform and isotropic total surface stress will give rise to in-plane deformation of the unrestrained plate. Solution to the corresponding displacement field of this plate is given by

$$u(x_1) = \frac{-(1-\nu)}{Eh}\,\sigma_s^T x_1, \tag{1a}$$

$$v(x_2) = \frac{-(1-\nu)}{Eh}\,\sigma_s^T x_2, \tag{1b}$$

where u, v, E, ν, and h are the displacements in the x_1 and x_2-directions, Young's modulus, Poisson's ratio, and thickness, respectively. Importantly, other isotropic loads commonly encountered in practice can produce displacement fields in the x_1, x_2-plane that are identical to Eq. (1), including thermal and piezoelectric loads.[23,40,42,43]

We next consider the general problem of a thin isotropic linearly elastic plate whose edges can be free, simply supported, or clamped; a few examples are illustrated in Figs. 1(a) and 1(b). The unrestrained plate solution is used to calculate the deformation of the original (restrained) plate using the method of linear superposition.[27,28] This is achieved by decomposing the original plate problem into two subproblems as follows:

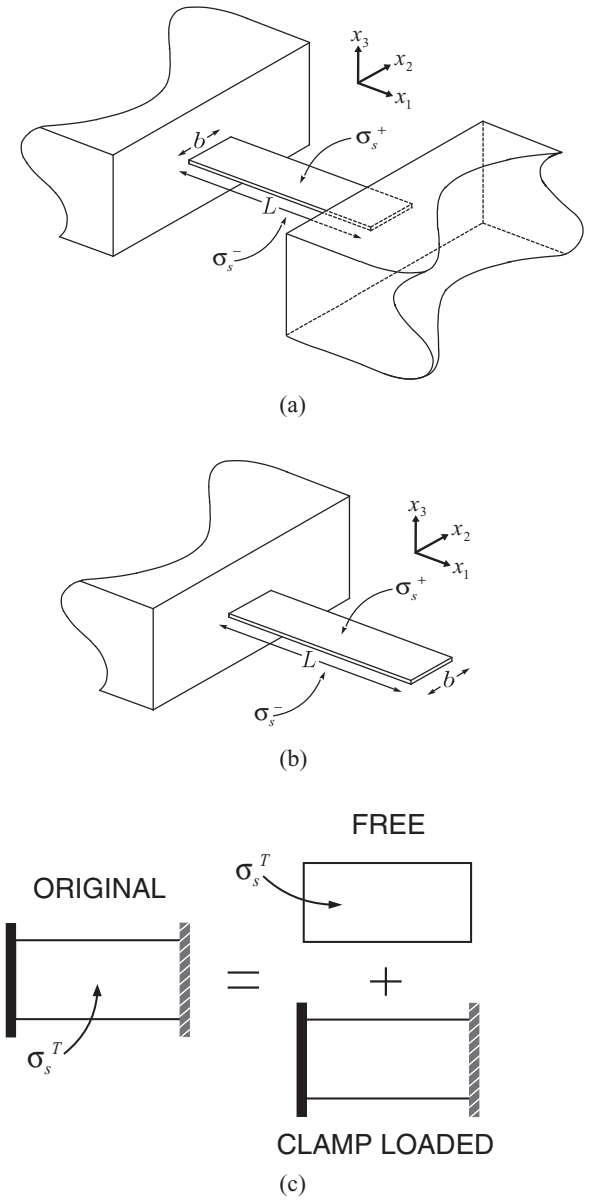

FIG. 1. Schematic of (a) a doubly-clamped beam and (b) a cantilever plate showing coordinate system and applied surface stresses. The origin of the coordinate system is at the center of mass of the doubly-clamped beam and the clamped end of the cantilever plate. Decomposition of original problem (c) highlights the removable clamp, present for doubly-clamped beams and removed for cantilever plates.

Subproblem (1): Deformation of the unrestrained plate under application of an isotropic surface stress load.

Subproblem (2): A plate with no imposed surface stress load but specified in-plane displacements at its restrained edges that are identical and opposite in sign to those obtained in subproblem (1). Addition of subproblems (1) and (2) thus ensures satisfaction of the original boundary conditions; see Fig. 1(c).

Superposition of these two subproblems yields an identical in-plane deformation to that of the original problem. The net in-plane stress of the original problem is captured by subproblem (2), since subproblem (1) is unrestrained. As such, the stiffness

change of the original problem is given by that of subproblem (2).

Importantly, subproblem (2) has displacement conditions at the restrained edge(s) and no-traction conditions at the free edge(s). This subproblem is, thus, a mixed boundary value problem that can pose a formidable challenge to calculate analytically, and numerical techniques may be required.

We now solve subproblem (2) for two cases of practical interest as follows:

(i) *Doubly-clamped beams*: Subproblem (1) produces an axial extension/contraction along the x_1-direction. This can be easily calculated by substituting the beam length L into Eq. (1a). Since this axial displacement is incommensurate with the boundary conditions at both ends of the original problem, subproblem (2) must involve an axial contraction/extension along the same longitudinal axis, i.e., $u = (1-\nu)\,\sigma_s^T L/(Eh)$; deformation in the x_2-direction is irrelevant since the beam length is assumed to greatly exceeds its width, in accord with Saint-Venant's principle.[43] In this case, subproblem (2) reduces to the axial loading of a thin beam, which can be solved using Euler-Bernoulli beam theory.

(ii) *Cantilever plates*: Subproblem (1) gives rise to an isotropic biaxial expansion/compression parallel to the plane of the plate. Since this violates the boundary condition at the restrained edge of the original cantilever plate, subproblem (2) contains a linear displacement along the clamp, i.e., $v = (1-\nu)\,\sigma_s^T\, x_2/(Eh)$. This displacement induces a complex in-plane stress distribution within the vicinity of the clamp. Such behavior can only be captured using a theory of higher order than Euler-Bernoulli beam theory; the latter inherently ignores the details in the immediate vicinity of the clamp. Here, a rigorous three-dimensional finite element analysis is used to solve subproblem (2); see Sec. III.

A scaling analysis for this problem is presented in Sec. II B to elucidate the dominate physical mechanisms. It is also used to generalize the numerical results.

A. Subproblem (2): Doubly-clamped beams

We now derive analytical expressions for the relative frequency shift and relative change in effective spring constant of doubly-clamped beams.

To begin, consider the governing equation of an Euler-Bernoulli beam under axial loading,

$$\frac{EI}{L^4}\frac{\partial^4 w}{\partial X^4} - \frac{T}{L^2}\frac{\partial^2 w}{\partial X^2} + \mu\frac{\partial^2 w}{\partial t^2} = 0, \tag{2}$$

where $X \equiv x_1/L$ is the scaled axial distance, t is time, w the beam deflection in the x_3-direction, I the second moment of area, T the axial load, and μ the linear mass density. Since geometric nonlinearities are ignored, the axial load T is decoupled from the out-of-plane deflection of the beam.[44] In this case, the axial displacement of subproblem (2) induces the axial load,

$$T = (1-\nu)\sigma_s^T b,$$

where b is the beam width. This axial load can then affect the stiffness and, hence, the resonant frequency of the beam.

1. Resonant frequency

We, first, calculate the change in resonant frequency due to an applied surface stress load. The case of an infinitesimal load is considered, which allows for calculation of the leading-order change in resonant frequency. This is obtained by expressing the deflection function in terms of the explicit time dependence $\exp(-i\omega t)$, where ω is the resonant frequency in the presence of an arbitrary surface stress, i.e., $w(X,t) = W(X)\exp(-i\omega t)$. Substituting $w(X,t)$ into Eq. (2) and cross-multiplying the resulting equations in both the presence and absence of surface stress, with the deflections $W_0(X)$ and $W(X)$, leads to

$$\omega^2 = \frac{EI}{\mu L^4}\left[\frac{\int_0^1 W_0''(X)^2\,dX}{\int_0^1 W_0(X)^2\,dX} - \frac{TL^2}{EI}\frac{\int_0^1 W_0(X)W''(X)\,dX}{\int_0^1 W_0(X)W(X)\,dX}\right], \tag{3}$$

where $W(X)$ and $W_0(X)$ are the dynamic deflection functions in the presence and absence of surface stress, respectively. To calculate the leading-order effect of surface stress on the fundamental mode resonant frequency, we replace the fundamental mode dynamic deflection function $W(X)$ in Eq. (3) with $W_0(X)$. The required expression for the relative frequency shift then immediately follows,

$$\frac{\Delta\omega}{\omega_0} = 0.1475\frac{(1-\nu)\sigma_s^T}{Eh}\left(\frac{L}{h}\right)^2, \tag{4}$$

where ω_0 is the (reference) resonant frequency in the absence of surface stress and $\Delta\omega = \omega - \omega_0$.

Equation (4) demonstrates that a positive (tensile) surface stress increases the stiffness of doubly-clamped beams; a negative (compressive) surface stress decreases the stiffness. It is also found that the length-to-thickness ratio L/h has a quadratic dependence on beam stiffness. This illustrates that increasing the length or reducing the thickness will enhance the sensitivity of doubly-clamped beams to surface stress. Interestingly, we find that Eq. (4) depends on Poisson's ratio. This may appear surprising at first, given that the deflection function for elementary beam theory does not depend on Poisson's ratio. However, the axial load giving rise to this effect originates from a biaxial strain in the plate. This is the origin of the observed Poisson's ratio dependence.

2. Effective spring constant

To calculate the change in effective spring constant of a beam due to a change in surface stress, we first consider the potential energy of the beam due to a distributed lateral load q. Using a similar approach to the resonant frequency above, we now consider the Euler-Bernoulli beam equation for static deflection, which yields

$$\int_0^1 q w(X)\,dX = \int_0^1 q w_0(X)\,dX + \frac{T}{L^2}\int_0^1 w_0(X)w''(X)\,dX, \tag{5}$$

where $w_0(X)$ and $w(X)$ refer to the static mode deflection functions in the presence of surface stress and in its absence, respectively. We again consider the case of infinitesimal loads and, thus, calculate the leading-order change in effective stiffness. This is obtained by replacing the static deflection function $w(X)$ on the right-hand side of Eq. (5) by $w_0(X)$. In

addition, ignoring geometric nonlinearities and considering a point load at the center of the beam results in its deflection being inversely proportional to its stiffness at that position. These simplifications then lead to the required expression

$$\frac{\Delta k_{\text{eff}}}{k_0} = \frac{3}{10}\frac{(1-\nu)\sigma_s^T}{Eh}\left(\frac{L}{h}\right)^2, \tag{6}$$

where k_0 is the (reference) effective spring constant, $\Delta k_{\text{eff}} = k_{\text{eff}} - k_0$, and k_{eff} is the effective spring constant when arbitrary surface stresses are imposed.

Equation (6) demonstrates that the relative change in the effective spring constant has an identical scaling dependence to Eq. (4) for the resonant frequency shift, as expected. Comparing Eq. (4) to Eq. (6) establishes that the relative change in spring constant and resonant frequency shift differ by a factor of 2.03. The slight increase from the usual value of 2 expected from elementary mechanics results from the difference in mode shape for the static and dynamic cases.

In the next section we present a scaling analysis for cantilever plates under surface stress loads.

B. Scaling analysis for cantilever plates

We begin by considering the (two-dimensional) governing equation for the small deflection of a thin plate, subject to an arbitrary in-plane load,

$$D\frac{\partial^2}{\partial x_i\,\partial x_i}\left(\frac{\partial^2 w}{\partial x_j\,\partial x_j}\right) - N_{ij}\frac{\partial^2 w}{\partial x_i\,\partial x_j} = q, \tag{7}$$

where w is the plate deflection in the x_3-direction (that now depends on x_1 and x_2), D is the flexural rigidity, N is the in-plane stress tensor, and q is the applied load per unit area.

Since all nonlinearities are also ignored for cantilever plates, the in-plane stress problem is decoupled from the out-of-plane deflection.[42,44,45] Solution to this in-plane problem is obtained by solving the equations of equilibrium $\partial_i N_{ij} = 0$ and compatibility condition $\partial_{ii} N_{jj} = 0$.[42,43,46]

In accordance with Saint-Venant's principle, the strain applied at the clamped edge induces localized nonzero in-plane stresses that decay along the length of the cantilever, with a characteristic length scale b. This results in nonzero in-plane stress confined within a region near the clamp [$x_1 < O(b)$], outside of which is zero. From the boundary conditions of subproblem (2), the in-plane stress obeys the scaling relation $N \sim O(\bar{\sigma} Eh)$, where

$$\bar{\sigma} \equiv \frac{(1-\nu)\,\sigma_s^T}{Eh}. \tag{8}$$

Substituting this scaling relation for N into Eq. (7) reveals that the effective flexural rigidity is altered only in the region $x_1 < O(b)$. For $x_1 > O(b)$, the effective rigidity is unaffected. The overall change in stiffness is, thus, induced by a localized perturbation to the governing equation in the immediate vicinity of the clamp.

The scaling behavior of this effective flexural rigidity in the region $x_1 < O(b)$ is, therefore, $D_{\text{eff}}/D_0 - 1 \sim O[\bar{\sigma}(b/h)^2]$, where D_{eff} is the effective flexural rigidity and D_0 the (unloaded) flexural rigidity of the cantilever plate. As the aspect ratio L/b increases, the effect of the in-plane load decreases, since the region containing nonzero in-plane stress is reduced relative to the entire region of the cantilever. Since the in-plane load affects the plate rigidity only in the region where $x_1 < O(b)$, it then follows that the leading-order behavior of the (total) effective rigidity is captured by

$$\frac{D_{\text{eff}}}{D} - 1 \sim O\left[\bar{\sigma}\left(\frac{b}{L}\right)\left(\frac{b}{h}\right)^2\right] \tag{9}$$

in the limit $L/b \gg 1$.

In the next section we present numerical solutions to subproblem (2) for cantilever plates. The underlying physical mechanisms driving the stiffness change in cantilever plates are also explored.

III. RESULTS AND DISCUSSION

We solved subproblem (2) for a cantilever plate using a full three-dimensional finite element analysis.[47] The mesh was systematically refined to ensure a convergence of 98%. Results are presented for a wide range of geometries, which correspond to width ratios between $16 \leqslant b/h \leqslant 48$ and aspect ratios $2 < L/b \leqslant 100$. The effect of nonzero Poisson's ratio is also investigated over the practical range $0 \leqslant \nu \leqslant 0.49$. Using the above scaling analysis allows for appropriate normalization of the numerical data in the asymptotic limit as $L/b \to \infty$.

As discussed above, we consider two complementary approaches to examine the effect of surface stress on cantilever stiffness: (i) Apply a fixed load at the tip and observe changes in the static deflection; this subsequently allows for calculation of changes in the effective spring constant k_{eff}. (ii) Use an eigenvalue analysis to obtain the resonant frequency ω of the cantilever plate; explicit results for the latter case were presented in Ref. 27. Here, we expand on that previous study[27] and present a detailed analysis for both approaches.

A. Subproblem (2): Cantilever plates

Equation (9) gives the leading-order scaling behavior for the effective rigidity D_{eff} as a function of surface stress. Since cantilever stiffness is proportional to the effective rigidity D_{eff}, the leading-order dependence of both the relative change in the effective spring constant and relative frequency shift inherently yield identical scaling behavior.

For the relative change in resonant frequency ω, we obtain

$$\frac{\Delta\omega}{\omega_0} = \phi_\omega(\nu)\bar{\sigma}\left(\frac{b}{L}\right)\left(\frac{b}{h}\right)^2, \tag{10}$$

where ω_0 is the resonant frequency in the absence of an applied surface stress load, $\Delta\omega = \omega - \omega_0$, and $\phi_\omega(\nu)$ is a function purely dependent on Poisson's ratio ν.

Similarly, the general expression for the relative change in the effective spring constant k_{eff} is

$$\frac{\Delta k_{\text{eff}}}{k_0} = \phi_k(\nu)\bar{\sigma}\left(\frac{b}{L}\right)\left(\frac{b}{h}\right)^2, \tag{11}$$

where k_0 is the effective spring constant without a surface stress load, $\Delta k_{\text{eff}} = k_{\text{eff}} - k_0$, and $\phi_k(\nu)$ is another function purely dependent on Poisson's ratio ν. These expressions are derived in the asymptotic limit $L \gg b \gg h$. The unknown functions, which depend only on Poisson's ratio, are now evaluated.

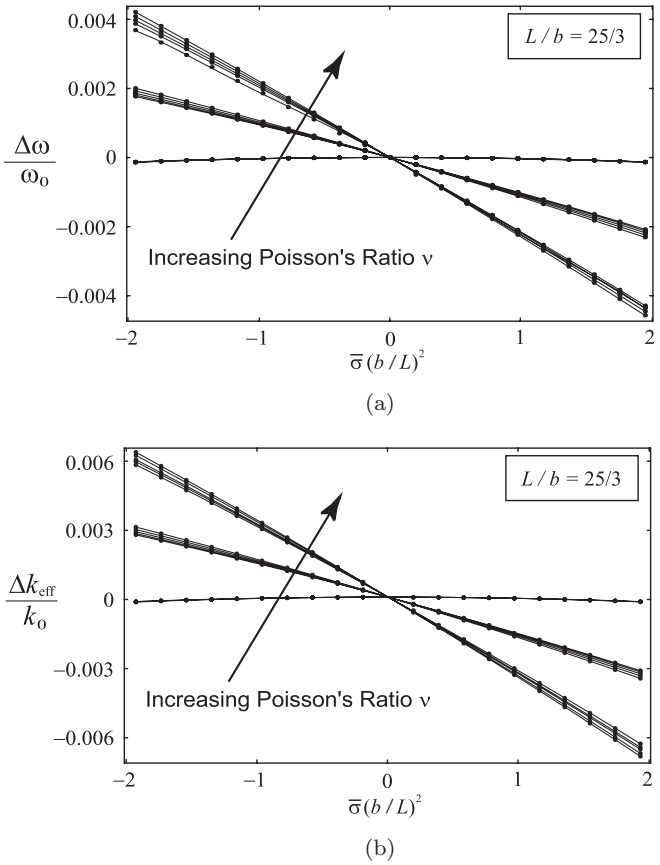

FIG. 2. Results for (a) relative frequency shift $\Delta\omega/\omega_0$ vs. $\bar{\sigma}(b/h)^2$ and (b) relative change in effective spring constant $\Delta k_{\text{eff}}/k_0$ vs. $\bar{\sigma}(b/h)^2$ for $L/b = 25/3$. Both figures show three groups of Poisson's ratio: $\nu = 0, 0.25, 0.49$. Each group contains $b/h = 16, 19.2, 24, 32, 48$.

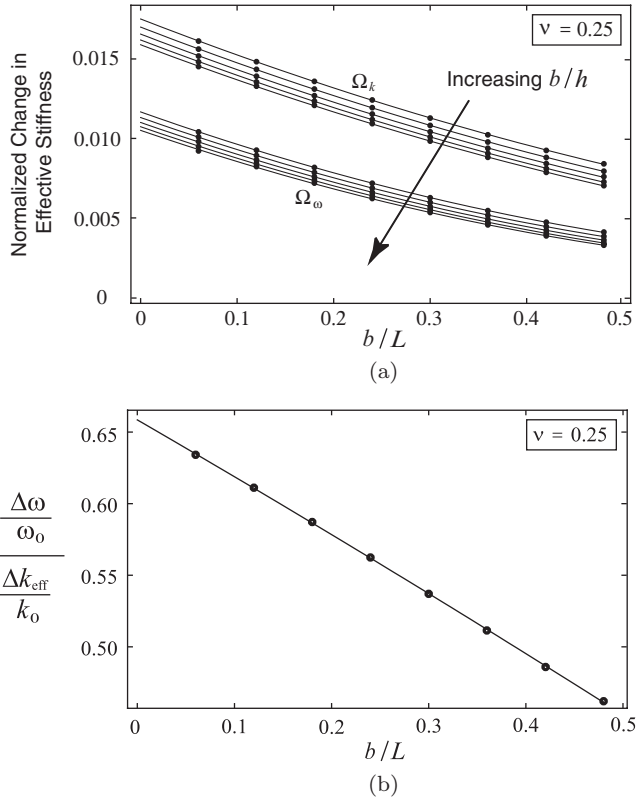

FIG. 3. (a) Results for normalized frequency shift $\Omega_\omega \equiv |\Delta\omega_{\text{lin}}/\omega_0|/|\bar{\sigma}(b/L)(b/h)^2|$ and normalized change in effective spring constant $\Omega_k \equiv |\Delta k_{\text{lin}}/k_0|/|\bar{\sigma}(b/L)(b/h)^2|$; $b/h = 16, 19.2, 24, 32, 48$; $\nu = 0.25$. Subscript "lin" indicates the result from linear regression. (b) Relationship between resonant frequency shift and change in effective spring constant $(\Delta\omega/\omega_0)/(\Delta k_{\text{eff}}/k_0)$ vs. b/L. Results extrapolated to zero thickness; $\nu = 0.25$.

Figure 2 presents numerical results for both the relative change in resonant frequency and effective spring constant; both cases have been scaled with $(b/h)^2$, in accordance with Eqs. (10) and (11). Figure 2 demonstrates that Eqs. (10) and (11) accurately capture the dominate width ratio b/h dependence, for both the resonant frequency ω and effective spring constant k_{eff}, with all curves collapsing for a given Poisson's ratio ν. It is also evident that the effective stiffness depends strongly on Poisson's ratio, with increasing ν enhancing the effect. We investigate the mechanism behind this Poisson's ratio dependence in Sec. III B.

Importantly, Fig. 2 includes all nonlinear effects, which are ignored in the formulation of Eqs. (10) and (11). Consequently, to make a quantitative and rigorous comparison to Eqs. (10) and (11) and evaluate $\phi_\omega(\nu)$ and $\phi_k(\nu)$, we henceforth extract the linear portion of these numerical results using linear regression and report these results only.

In Fig. 3(a), we illustrate the aspect ratio L/b dependence predicted in Eqs. (10) and (11). Results are presented for a range of aspect ratios L/b, Poisson's ratio $\nu = 0.25$, with width ratios b/h corresponding to those used in Fig. 2. Results for other nonzero Poisson's ratios are similar to those in Fig. 3(a), while differing in magnitude. The vertical axis is scaled in accordance with Eqs. (10) and (11) to explore their validity. From Fig. 3(a), it is clear that Eqs. (10) and (11) also capture the dominant aspect ratio dependence for large L/b, which is the regime in which they were derived, while a higher-order dependence on aspect ratio is also visible for smaller L/b; this higher-order dependence can be calculated from the results in Fig. 3(a), if required. These results confirm the validity of the scaling argument behind Eqs. (10) and (11) for small surface stress loads.

Figure 3(b) demonstrates the aspect ratio L/b dependence of the ratio between the resonant frequency shift and relative change in effective spring constant, i.e., $(\Delta\omega/\omega_0)/(\Delta k_{\text{eff}}/k_0)$. Since Eqs. (10) and (11) were derived within the framework of the classical theory of thin plates, numerical results for each aspect ratio L/b are extrapolated to the zero thickness limit, $h/b \to 0$. Figure 3(b) illustrates that in the formal limit, $L/b \to \infty$, this ratio becomes $(\Delta\omega/\omega_0)/(\Delta k_{\text{eff}}/k_0) \approx 2/3$. This contrasts to doubly-clamped beams, where the relative change in resonant frequency and effective spring constant differ by a factor of 2.03. The mechanism giving rise to this factor of 2/3 is explored in detail in Sec. III C.

To determine the functions $\phi_\omega(\nu)$ and $\phi_k(\nu)$ in Eqs. (10) and (11), numerical data for the resonant frequency shift and relative change in effective spring constant are extrapolated in the binary limit $L/b \to \infty$ and $b/h \to \infty$. This is precisely the regime in which these asymptotic expressions are formulated. Given the linearity of the data in this limit, extrapolation

is robust and accurate. Results for various Poisson's ratio are then used to evaluate $\phi_\omega(\nu)$ and $\phi_k(\nu)$. We find that both $\phi_\omega(\nu)$ and $\phi_k(\nu)$ vary approximately linearly with Poisson's ratio and are well described by $\phi_\omega(\nu) \approx -0.042\nu$ and $\phi_k(\nu) \approx -0.063\nu$ for the resonant frequency and effective spring constant, respectively. Substituting $\phi_\omega(\nu)$ into Eq. (10) and $\phi_k(\nu)$ into Eq. (11) gives the required resonant frequency shift,

$$\frac{\Delta\omega}{\omega_0} = -0.042\nu\,\bar{\sigma}\left(\frac{b}{L}\right)\left(\frac{b}{h}\right)^2, \tag{12}$$

and relative change in effective spring constant,

$$\frac{\Delta k_{\text{eff}}}{k_0} = -0.063\nu\,\bar{\sigma}\left(\frac{b}{L}\right)\left(\frac{b}{h}\right)^2. \tag{13}$$

We emphasize that these results are consistent with the null result of Gurtin *et al.*,[25] that was derived in the formal limit $L/b \to \infty$ using classical beam theory. In this limit, Eqs. (12) and (13) also predict that surface stress loads have no effect on the stiffness. The mechanism giving rise to stiffness change due to surface stress lies in the development of localized in-plane loads near the clamp, which are inherently ignored in beam theory. This also yields the observed Poisson's ratio dependence that only can be captured using a theory of higher dimension, such as thin plate theory.

We now examine the mechanism underlying (i) the observed Poisson's ratio dependence, and (ii) the observed ratio between the relative frequency shift and relative change in effective spring constant, $(\Delta\omega/\omega_0)/(\Delta k_{\text{eff}}/k_0) \approx 2/3$ for $L/b \gg 1$.

B. Poisson's ratio dependence

To examine the origin of the Poisson's ratio dependence on effective stiffness, we derive an analytical expression for the leading-order change in resonant frequency of a cantilever plate. To begin, consider the governing equation of a thin plate under in-plane loading

$$D\frac{\partial^2}{\partial x_i\,\partial x_i}\left(\frac{\partial^2 w}{\partial x_j\,\partial x_j}\right) - N_{ij}\frac{\partial^2 w}{\partial x_i\,\partial x_j} + \rho h\frac{\partial^2 w}{\partial t^2} = 0, \tag{14}$$

where w is the deflection function in the x_3-direction and ρ is the plate density. By again considering an explicit time dependence of $\exp(-i\omega t)$, the deflection function becomes $w(x_1,x_2,t) = W(x_1,x_2)\exp(-i\omega t)$. Substituting $w(x_1,x_2,t)$ into Eq. (14), and cross-multiplying the resulting equations for the two cases where in-plane loads are present and absent, with the deflections W_0 and W, respectively, yields

$$\omega^2 - \omega_0^2 = -\frac{\iint_S W_0 N_{ij}\partial_{ij} W\,dS}{\rho h\iint_S W_0 W\,dS}, \tag{15}$$

where W and W_0 are the deflection functions in the presence of in-plane loads and in their absence, respectively; the integrals are over the surface S of the plate. Since infinitesimal in-plane loads are applied, the leading-order change in the fundamental mode resonant frequency is obtained by replacing W in Eq. (15) with W_0. This then leads to

$$\Delta\omega = -\frac{1}{2M}\iint_S W_0 N_{ij}\partial_{ij} W_0\,dS, \tag{16}$$

where $\Delta\omega = \omega - \omega_0$ is now the leading-order change in resonant frequency due to small changes in surface stress, where M is

$$M = \omega_0\rho h\iint_S W_0^2\,dS$$

and

$$\omega_0^2 = \frac{D\iint_S W_0\partial_{ii}\partial_{jj} W_0\,dS}{\rho h\iint_S W_0^2\,dS}. \tag{17}$$

Equation (16) clearly shows coupling between the deflection function and the in-plane stresses. Modification of either term can potentially change the cantilever stiffness. In the following discussion, we examine the importance of each term in Eq. (16) to elucidate the origin of the Poisson's ratio dependence observed in Eqs. (12) and (13).

1. Zero Poisson's ratio

For $\nu = 0$, the deflection function, W_0, is independent of x_2 and identical to the result from Euler-Bernoulli beam theory. The change in resonant frequency for $\nu = 0$, therefore, simplifies to give

$$\Delta\omega|_{\nu=0} = -\frac{1}{2M}\int_0^L \frac{d^2 W_0}{dx_1^2} W_0\left(\int_{-\frac{b}{2}}^{\frac{b}{2}} N_{11}\,dx_2\right)dx_1. \tag{18}$$

We next prove that the above integral of N_{11} with respect to x_2 is zero. Consider a rectangular region within the plate, with three sides coinciding with the free edges, and an arbitrary slice in the interior of the plate; see Fig. 4. The equilibrium equation, $\partial_i N_{ij} = 0$, is integrated over this rectangular region. Use of the divergence theorem then yields

$$\iint_{S_1}\frac{\partial N_{ij}}{\partial x_i}dS_1 = \oint_{\partial C} N_{ij}\hat{n}_i dC = 0, \tag{19}$$

where $\hat{n}_i$ is the outward normal to the boundary. Applying the usual no-traction boundary condition, $N_{ij}\hat{n}_i = 0$, along the free edges reduces the integral on the right-hand side of Eq. (19) to

$$\hat{\mathbf{x}}_1\int_{-\frac{b}{2}}^{\frac{b}{2}} N_{11}dx_2 + \hat{\mathbf{x}}_2\int_{-\frac{b}{2}}^{\frac{b}{2}} N_{12}dx_2 = \mathbf{0}, \tag{20}$$

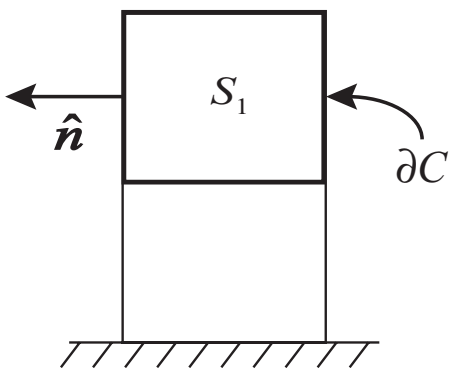

FIG. 4. Plan view of cantilever plate showing rectangular region within interior; this specifies the boundary of integration used to prove the stiffness change vanishes for zero Poisson's ratio.

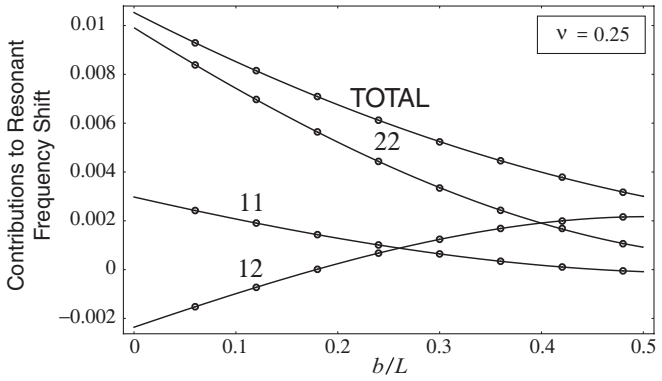

FIG. 5. Normalized relative change in resonant frequency, TOTAL $\equiv \Omega\Delta\omega/\omega_0$, and its normalized components, $11 \equiv \Omega\Delta\omega_{11}/\omega_0$, $22 \equiv \Omega\Delta\omega_{22}/\omega_0$, and $12 \equiv \Omega\Delta\omega_{12}/\omega_0$, plotted against b/L, where $\Omega = -1/\{\bar{\sigma}(b/L)(b/h)^2\}$; $h/b \to 0$, $\nu = 0.25$.

where $\hat{\mathbf{x}}_1$ and $\hat{\mathbf{x}}_2$ are unit vectors in the x_1 and x_2-directions, respectively. This establishes that the integral of N_{11} with respect to x_2 is zero. Substituting this result into Eq. (18) proves that a Poisson's ratio of zero yields no change in the resonant frequency of the plate. This verifies the empirically derived result in Fig. 2 for $\nu = 0$, from which a negligible variation in stiffness for an arbitrary in-plane load was observed.

2. *Nonzero Poisson's ratio*

In the case of nonzero Poisson's ratio, the deflection function depends on x_2. Therefore, the above analysis for zero Poisson's ratio no longer holds. Thus, all terms in the integral of Eq. (16) can potentially be nonzero. To investigate the contribution of each term in Eq. (16), we expand the relative change in resonant frequency as

$$\frac{\Delta\omega}{\omega_0} = \frac{\Delta\omega_{11}}{\omega_0} + \frac{\Delta\omega_{12}}{\omega_0} + \frac{\Delta\omega_{22}}{\omega_0}, \tag{21}$$

where

$$\Delta\omega_{11} = -\frac{1}{2M}\iint_S N_{11}\frac{\partial^2 W_0}{\partial x_1^2} W_0\, dS, \tag{22a}$$

$$\Delta\omega_{22} = -\frac{1}{2M}\iint_S N_{22}\frac{\partial^2 W_0}{\partial x_2^2} W_0\, dS, \tag{22b}$$

$$\Delta\omega_{12} = -\frac{1}{M}\iint_S N_{12}\frac{\partial^2 W_0}{\partial x_1\,\partial x_2} W_0\, dS. \tag{22c}$$

The expressions in Eqs. (22) define contributions from each in-plane stress component N_{ij} to the total frequency shift. Note that each contribution results from coupling between the in-plane stress, deflection function, and curvature.

Using our full three-dimensional model, we now numerically evaluate each term in Eq. (21). As in Ref. 27, results are first computed for finite thickness cantilever plates. The numerical data are then extrapolated to zero thickness to obtain the required results that are consistent with thin plate theory.[27] Results in Fig. 5 are given for a Poisson's ratio of $\nu = 0.25$ and illustrate the contributions from each term in Eq. (21) to the overall frequency shift. Figure 5 demonstrates that each term in Eq. (21) exhibits an approximate linear dependence on b/L, provided $b/L \ll 1$; higher-order effects are clearly present for $b/L > 0.3$. This reveals that the components of the change in resonant frequency have a significant dependence on aspect ratio, L/b. From the results in Fig. 5, it is evident that the dominant contribution for large L/b is given by $\Delta\omega_{22}$, with $\Delta\omega_{11}$ and $\Delta\omega_{12}$ playing a relatively minor role. Note that $\Delta\omega_{11}$ and $\Delta\omega_{12}$ are approximately equal and opposite in magnitude for $b/L < 0.3$. The following analysis will, thus, focus only on the dominant component, $\Delta\omega_{22}$, for $L/b \gg 1$.

a. Contribution from $\Delta\omega_{22}$. Since the resonant frequency ω_0 and deflection function w_0 are insensitive to Poisson's ratio ν, for $L \gg b$, it then follows that M will also be insensitive to ν; this feature has been verified numerically. Thus, M cannot lead to the observed Poisson's ratio dependence in Fig. 2.

Results for the normalized in-plane stress, $\overline{N} \equiv N_{22}/(\bar{\sigma}Eh)$, are presented in Fig. 6(a) for $\nu = 0.25$. Figure 6(a) demonstrates that the uniform strain applied along the clamp induces a nonuniform stress distribution in the vicinity of the clamp. Since the in-plane stress distribution decays rapidly for $x_1 > 2b$, Fig. 6(a) gives the distribution for all aspect ratios, $L/b > 2$. To examine the Poisson's ratio dependence on $\overline{N}$, Fig. 6(b) gives the difference between the normalized in-plane stress $\overline{N}$ for $\nu = 0.25$ and 0.49. Interestingly, Fig. 6(b) reveals that the contours of the normalized in-plane stress, $\overline{N}$, are virtually unaffected by Poisson's ratio. This establishes that N_{22} also does not contribute to the linear Poisson's ratio dependence observed in Fig. 2.

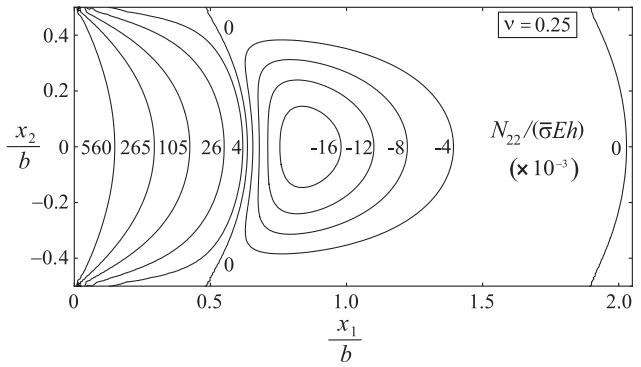

FIG. 6. (a) Normalized in-plane stress $\overline{N} \equiv N_{22}/(\bar{\sigma}Eh)$ for $\nu = 0.25$ and (b) difference between the normalized in-plane stress $\overline{N}$ for $\nu = 0.25$ and 0.49; $x_1 < 2b$. Actual contour values are 10^{-3} times those given in both figures. Results given for aspect ratio $L/b = 2$.

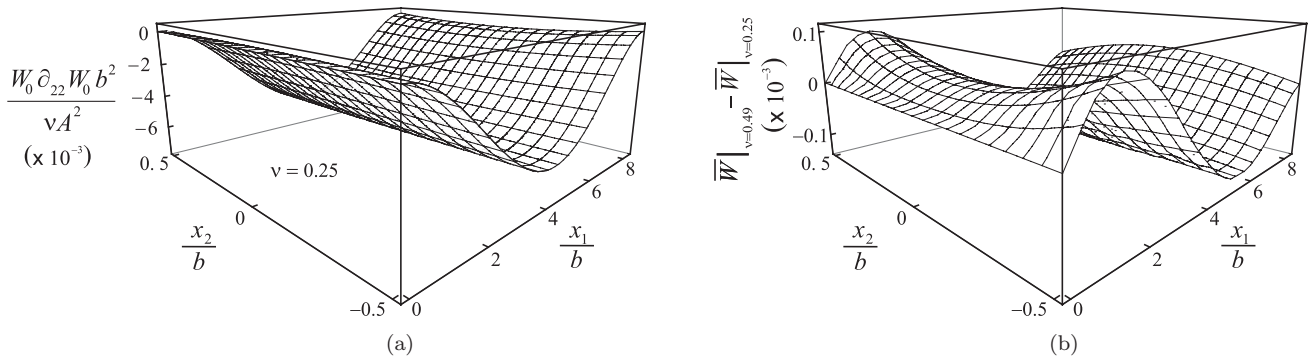

FIG. 7. (a) Scaled product of dynamic deflection and curvature in the x_2-direction, $\overline{W} \equiv W_0\partial_{22}W_0 b^2/(\nu A^2)$, for $\nu = 0.25$. (b) Difference between the scaled product of dynamic deflection and curvature, $\overline{W}$, for $\nu = 0.25$ and 0.49. The deflection function, W_0, has been normalized by its amplitude, A, at the center of the free-end of the cantilever, i.e., $(x_1,x_2) = (L,0)$. The coordinate x_2 is scaled by b. Both cases shown over entire length for an aspect ratio of $L/b = 25/3$. The vertical axis is scaled by 10^{-3}.

We, thus, turn our attention to variations in the deflection function of the cantilever plate. In Fig. 7(a), we give results for the scaled product of the dynamic deflection and curvature in the x_2-direction, $W_0\partial_{22}W_0$, for a Poisson's ratio of $\nu = 0.25$; the contribution of this component to the total frequency shift is specified by Eq. (22b). Results are given for the fundamental mode of vibration only. To assess the Poisson's ratio dependence of $W_0\partial_{22}W_0$, Fig. 7(b) plots the difference between the scaled product of dynamic deflection and curvature for $\nu = 0.25$ and 0.49. Significantly, this difference is an order of magnitude smaller than the results in Fig. 7(a). This establishes that the dominant mechanism underlying the linear Poisson's ratio dependence results from coupling of N_{22} with the Poisson's ratio dependence of the deflection function – N_{11} and N_{12} play a relatively minor role. This finding is consistent with the proof in Sec. III B 1 that N_{22} does not contribute to the change in stiffness when Poisson's ratio is zero.

In the next section, we investigate the origin of the observed ratio between the relative frequency shift and relative change in effective spring constant.

C. Relationship between frequency shift and effective spring constant

The numerical results in Fig. 3(b) demonstrate that the ratio of the relative frequency shift and relative change in effective spring constant approaches 2/3 as the aspect ratio L/b tends to infinity; i.e., $(\Delta\omega/\omega_0)/(\Delta k_{\text{eff}}/k_0) \to 2/3$. This differs from the result for doubly-clamped beams and from what is naively expected from elementary mechanics. The underlying mechanism giving rise to this unexpected behavior for cantilever plates is now explored. To begin, we introduce analytical formulas for the relative frequency shift and relative change in effective spring constant. These are obtained for small surface stress changes.

The formula for the relative frequency shift follows immediately from Eqs. (16) and (17):

$$\frac{\Delta\omega}{\omega_0} = -\frac{1}{2}\frac{\iint_S W_0 N_{ij}\partial_{ij}W_0\,dS}{D\iint_S W_0\partial_{ii}\partial_{jj}W_0\,dS}. \tag{23}$$

The change in effective spring constant of a cantilever plate is derived by considering the potential energy of the plate due to a lateral load q. By using a similar approach to the resonant frequency above, we consider the governing equation of a thin plate for static deflection, which immediately gives

$$\iint_S q w\,dS - \iint_S q w_0\,dS = \iint_S w_0 N_{ij}\frac{\partial^2 w}{\partial x_i\partial x_j}\,dS, \tag{24}$$

where w and w_0 are the static deflection functions when in-plane loads are present and absent, respectively. If infinitesimal loads are again imposed on the plate, the leading-order relative change in effective stiffness is obtained by replacing the deflection w on the right-hand side of Eq. (24) with w_0. Furthermore, if a lateral force per unit length is applied along the width of the cantilever tip, the deflection at that position will be inversely proportional to the effective stiffness at that position, which leads to

$$\frac{\Delta k_{\text{eff}}}{k_0} = -\frac{\iint_S w_0 N_{ij}\partial_{ij}w_0\,dS}{D\iint_S w_0\partial_{ii}\partial_{jj}w_0\,dS}, \tag{25}$$

where $\Delta k_{\text{eff}} = k_{\text{eff}} - k_0$ is now the leading-order change in the effective spring constant.

Next, to obtain an analytical expression for the relationship between the relative resonant frequency shift and relative change in effective spring constant, we take the ratio of Eq. (23) and Eq. (25), i.e.,

$$\frac{\frac{\Delta\omega}{\omega_0}}{\frac{\Delta k_{\text{eff}}}{k_0}} = \frac{1}{2}\frac{\Delta\Pi}{\Pi_0}, \tag{26}$$

where

$$\Pi_0 = \frac{\iint_S W_0\partial_{ii}\partial_{jj}W_0\,dS}{\iint_S w_0\partial_{ii}\partial_{jj}w_0\,dS}, \tag{27}$$

is the ratio between the dynamic and static spring constant in the absence of in-plane loads and

$$\Delta\Pi = \frac{\iint_S W_0 N_{ij}\partial_{ij}W_0\,dS}{\iint_S w_0 N_{ij}\partial_{ij}w_0\,dS}, \tag{28}$$

is the contribution of the in-plane stress N_{ij}. In the asymptotic limit, $L/b \to \infty$, the ratio between the dynamic and static spring constant is $\Pi_0 = 1.03$. As such, for $L \gg b$, the value of Π_0 can be rounded off to unity without introducing significant errors in Eq. (26). We now turn our attention to $\Delta\Pi$.

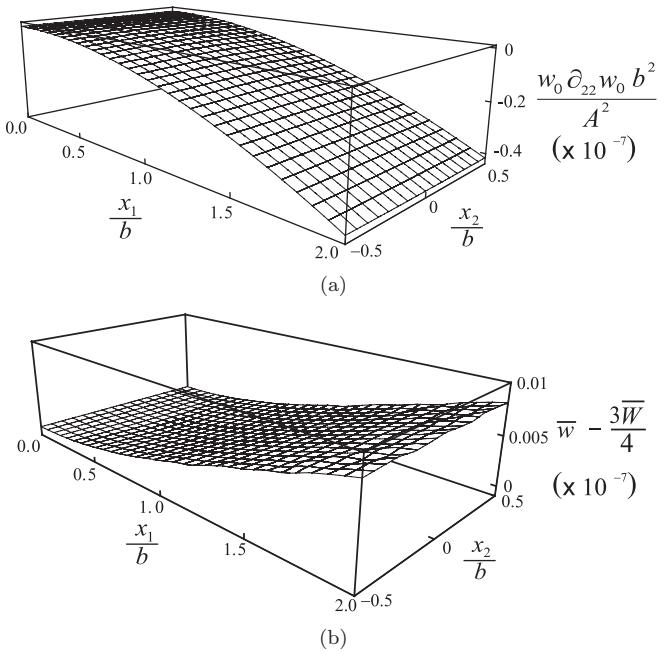

FIG. 8. (a) Scaled product of static deflection and curvature in the x_2-direction, $\overline{w} \equiv w_0 \partial_{22} w_0 b^2/A^2$. (b) Difference between the scaled product of static deflection and curvature, $\overline{w}$, and 3/4 times the scaled product of dynamic deflection and curvature, $\overline{W} \equiv W_0 \partial_{22} W_0 b^2/A^2$; $L/b = 100$, $x_1 \leqslant 2b$. The deflection functions, w_0 and W_0, have been normalized by their amplitudes, A, at the center of the free-end of the cantilever, i.e., $(x_1,x_2) = (L,0)$. The coordinate x_2 is scaled by b and the vertical axis is scaled by 10^{-7}.

Since the in-plane loads in $\Delta\Pi$ are identical in the static and dynamic cases, and decay rapidly for $x_1 > O(b)$, we focus on contributions from the product of deflection and curvature in the immediate vicinity of the clamp; i.e., $x_1 < O(b)$. An example is given in Fig. 8(a) for the normalized product of static deflection and curvature, $w_0 \partial_{ij} w_0$, for $L/b \gg 1$. Near the clamp, all products of the deflection and curvature in the numerator (dynamic problem) of Eq. (28) differ by a factor of $\sim 4/3$ to the denominator (static problem), i.e., $W_0 \partial_{ij} W_0 \approx 4/3\, w_0 \partial_{ij} w_0$. This feature is highlighted in Fig. 8(b), which presents the relative difference between these products. Substituting the result $W_0 \partial_{ij} W_0 \approx 4/3\, w_0 \partial_{ij} w_0$ into Eq. (28), then gives $\Delta\Pi \approx 4/3$, which from Eq. (26) reproduces the numerical result of Fig. 3(b), i.e., $(\Delta\omega/\omega_0)/(\Delta k_{\text{eff}}/k_0) \approx 2/3$, for $L/b \gg 1$.

This analysis establishes that the difference in $\Delta\omega/\omega_0$ and $\Delta k_{\text{eff}}/k_0$ is due to variations in the local plate curvature near the clamp for the static and dynamic cases, respectively.

D. Comparison between doubly-clamped beams and cantilever plates

We now compare the relative sensitivity of doubly-clamped beams and cantilever plates to surface stress change. Throughout, we focus on the relative change in frequency. Taking the ratio of Eqs. (4) and (12) gives

$$\frac{\left(\frac{\Delta\omega}{\omega_0}\right)_{\text{Clamp-Clamp}}}{\left(\frac{\Delta\omega}{\omega_0}\right)_{\text{Cantilever}}} \approx \frac{-3.51}{\nu}\left(\frac{L}{b}\right)^3. \tag{29}$$

This relationship has a cubic dependence on aspect ratio L/b, which establishes that increasing the aspect ratio strongly enhances the sensitivity of doubly-clamped beams to surface stress change, in comparison to cantilever plates. We remind the reader that all calculations have been derived in the asymptotic limit where the plate width greatly exceeds its thickness.

It is also found that Poisson's ratio plays a significant role in Eq. (29). This is expected, since cantilever plates are insensitive to surface stress variations in the limit of zero Poisson's ratio (see Sec. III B); the frequency shift in doubly-clamped beams is much more weakly dependent on Poisson's ratio.

Equation (29) establishes that doubly-clamped beams offer superior sensitivity to surface stress effects in comparison to cantilever plates in the asymptotic limit $L \gg b$. The analogous expression to Eq. (29) for the change in stiffness is larger by a factor of 4/3 in the limit $L/b \to \infty$. The physical mechanisms underlying this factor are detailed above.

E. Practical implications

To conclude, we discuss the practical implications of the theoretical findings and models presented above. For completeness, we first summarize the discussion presented in Ref. 27, while elaborating on some pertinent points. We then explore potential future measurements on nanoscale devices that can make use of the presented theory.

Interestingly, the effective stiffness change in Eqs. (12) and (13) is controlled by the ratio of the modified surface stress $\nu(1-\nu)\sigma_s^T$ to the (reference) stiffness $K \equiv Eh^3L/b^3$, i.e., the stiffness probed with characteristic length b rather than cantilever length L. This demonstrates that changes in thickness h or width b have a stronger effect in comparison to varying the length L. This scaling dependence differs considerably to that of surface elasticity (strain-dependent surface stress) and can be used to identify the influence of strain-independent surface stress. Examining the scaling dependence of strain-independent and strain-dependent surface stress contributions on cantilever geometry may provide further understanding of underlying physical mechanisms driving stiffness changes in cantilever plates.

Static bending due to differential surface stresses could also be combined with Eqs. (12) and (13) to determine changes in the (intrinsic) surface stresses, i.e., σ_s^+ and σ_s^-. The accuracy of such measurements achievable in practice is contingent on the precision of the measured effective stiffness or resonant frequency. This generalizes the approach of Müller *et al.*,[41] who suggested this approach for thin circular plates.

Clearly, Eqs. (12) and (13) indicate that short cantilever aspect ratio and reduced thickness offer higher sensitivity to surface stress effects. Thus, miniaturization to nanoscale devices, under the constraint that the classical theory of elasticity still holds,[48] presents a promising avenue for future developments. We provide a theoretical example demonstrating the enhanced sensitivity to surface stress changes of such miniaturized devices in the discussion that follows.

1. Available and proposed measurements

We now compare the predictions of the above surface stress model to available experimental data and propose a series of experiments to provide further insight into this phenomenon.

In Ref. 21, modifications to the surface of a series of cantilevers was achieved by etching. This was shown to affect the resonant frequency of the devices; see Fig. 4 of Ref. 21. In that study,[21] resonant frequency shifts due to etching ranged from a few percent to nearly 100%. Based on their (unphysical) axial force model, discussed above, the frequency shifts corresponded to changes in surface stress of approximately 0.2 N/m; this was within the expected values for such etching processes. As discussed in Ref. 27, the present model grossly underpredicts the resonant frequency shifts for these surface stress values, yielding $\Delta\omega/\omega_0 \approx 10^{-4}$. Thus, the derived model is unable to explain the observations.

More recent experiments elaborated on these earlier reports through adsorption to the cantilever surface, which changed the surface stress.[15,16,19,20,32] Measured resonant frequency shifts were found to vary between studies, with reported values ranging from $\Delta\omega/\omega_0 \approx 0.002 - 0.06$. For example, in Ref. 32 gold-coated silicon rectangular cantilevers of dimensions $499 \times 97 \times 0.8\ \mu\text{m}^3$ displayed a resonant frequency shift up to $\Delta\omega/\omega_0 \approx 0.01$ following an amino-ethanethiol-gold adsorption binding event. The surface stress change was measured using the usual bending technique.[1] Good agreement was also found between the measured surface stress and the predictions of the (unphysical) axial force model for the first six modes of vibration. In contrast, our model in Eq. (12) predicts a surface stress change of $\sigma_s^T \approx -60$ N/m. Thus again, we are unable to account for these measurements. Analysis of the works of Refs. 15, 16, 19, and 20 yields a similar conclusion.

In Ref. 27, we also mentioned a number of other possible mechanisms leading to these experimental observations. Nonetheless, we must note the distinct possibility that these experimentally observed changes in cantilever stiffness are due to mechanism(s) that are unrelated to surface stress. While a change in surface stress was induced and a subsequent change in resonant frequency observed, the suggested "cause and effect" has not been proven. Further work is required to unravel the mechanism leading to these observations and permit a definitive statement to be made. To this end, we propose some measurements that accentuate the theoretical effects described in this article for strain-independent surface stress.

Modern materials, such as graphene, provide an ideal platform for investigating the effects of strain-independent surface stress. These ultrathin materials amplify the effects of surfaces, and theory predicts a dramatic enhancement in the resulting resonant frequency shifts. Recently, Zhang *et al.*[49] demonstrated that materials down to a bilayer of graphene, corresponding to a thickness 6 Å, behave in accord with continuum mechanics. We, therefore, explore the application of the above theory to devices made of such ultrathin materials.

Importantly, measurements of surface stress induced changes in doubly-clamped beams have not been reported – measurements have only been provided for piezoelectric induced stress.[40] Consider a doubly-clamped beam made of graphene of length 3.2 μm, width 0.8 μm, and thickness 0.6 nm. Applying a surface stress change to such a device, Eq. (4) yields a scaled frequency shift of $1/\sigma_s^T(\Delta\omega/\omega_0) \approx 3.8 \times 10^3$ m N^{-1}; increasing the thickness reduces this value in accordance with the square of the thickness change. Using a typical value of $\sigma_s^T \approx 1 \times 10^{-3}$ N/m[32] yields a relative frequency shift of $\Delta\omega/\omega_0 \approx 3.8$, which greatly exceeds the measurements reported in the literature for piezoelectric-induced stress.[40] While this value is beyond the limits of the present (linear) theory, it highlights the fact that miniaturization to the nano/atomic scale can enable gigantic tunability of the mechanical properties of these devices. Thus, measurements of surface stress change should be easily discernible on doubly-clamped beams made from ultrathin materials such as graphene.

Using a graphene cantilever of identical dimensions to the doubly-clamped device would result in a scaled frequency shift of $1/\sigma_s^T(\Delta\omega/\omega_0) \approx -4.1$ m N^{-1}, according to Eq. (29). While this effect is smaller than that predicted for the doubly-clamped device, it is orders of magnitude higher in comparison to that predicted for micron-scale cantilevers used in previous studies. For example, a surface stress change of $\sigma_s^T \approx -2.5 \times 10^{-3}$ N m^{-1} is required to induce a frequency shift of $\Delta\omega/\omega_0 \approx 0.01$ in cantilever devices of identical dimensions to the above doubly-clamped graphene device. Microscale cantilevers of dimensions used in Ref. 32 reporting this frequency shift require an unrealistic surface stress change of $\sigma_s^T \approx -60$ N m^{-1}, as discussed above. This comparison indicates that dynamic measurements on ultrathin devices should be highly sensitive to the effects of surface stress change. This provides a promising route to investigating the origin of observed changes in cantilever stiffness due to surface modification. Any deviations from the presented theory could then be studied independently to identify their origin.

IV. CONCLUSION

We have presented a general theoretical formalism to calculate the effect of surface stress change on the stiffness of thin plates with arbitrary boundary (edge) conditions. The utility of this formalism was demonstrated by application to both doubly-clamped beams and cantilever plates. In so doing, we established that the stiffness of these two configurations exhibits vastly different sensitivities to surface stress change.

Specifically, Poisson's ratio was found to dramatically affect the surface stress sensitivity of cantilever plates, in contrast to doubly-clamped beams that are relatively insensitive to Poisson's ratio. Furthermore, doubly-clamped beams were found to exhibit a much stronger dependence on surface stress in comparison to cantilever plates. This superior performance increases with increasing aspect ratio (length/width). The difference in the relative stiffness change and frequency shift in cantilever devices was also examined and found to be due to the difference in local curvature near the clamped end. Finally, we proposed and theoretically analyzed experiments aimed at elucidating the origin of the observed stiffness changes in cantilever devices. The findings of this study are expected to

be of value to the design and application of sensors that utilize the dynamic response of nanomechanical beam devices.

ACKNOWLEDGMENTS

The authors gratefully acknowledge support of the Australian Research Council Grants Scheme.

*jsader@unimelb.edu.au

[1] G. G. Stoney, Proc. R. Soc. London A **82**, 172 (1909).
[2] G. Hass and R. E. Thun, *Physics of Thin Films* (Academic Press, New York, 1966).
[3] S. Boskovic, J. W. M. Chon, P. Mulvaney, and J. E. Sader, J. Rheol. **46**, 891 (2002).
[4] H. Ibach, Surf. Sci. Rep. **29**, 193 (1997).
[5] M. Alvarez and L. M. Lechuga, Analyst **135**, 827 (2010).
[6] S. Sukuabol, D. K. Sood, and G. Rosengarten, *Proceedings of the 2005 Intelligent Sensors, Sensor Networks & Information Processing Conference* (IEEE, New York, 2005), p. 247.
[7] K. Eoma, H. S. Park, D. S. Yoonc, and T. Kwonc, Phys. Rep. **503**, 115 (2011).
[8] N. V. Lavrik, M. J. Sepaniak, and P. G. Datskos, Rev. Sci. Instrum. **75**, 2229 (2004).
[9] B. Gheshlaghi and S. M. Hasheminejad, Composites B **42**, 934 (2011).
[10] T. Thundat, E. A. Wachter, S. L. Sharp, and R. J. Warmack, Appl. Phys. Lett. **66**, 1695 (1995).
[11] D. Ramos, M. Arroyo-Hernández, E. Gil-Santos, H. D. Tong, C. van Rijn, M. Calleja, and J. Tamayo, Anal. Chem. **81**, 2274 (2009).
[12] J. Tamayo, D. Ramos, J. Mertens, and M. Calleja, Appl. Phys. Lett. **89**, 224104 (2006).
[13] D. Ramos, J. Mertens, M. Calleja, and J. Tamayo, Sensors **7**, 1757 (2007).
[14] R. Berger, E. Delamarche, H. P. Lang, C. Gerber, J. K. Gimzewski, E. Meyer, and H. J. Guntherodt, Science **276**, 2021 (1997).
[15] J. H. Lee, T. S. Kim, and K. H. Yoon, Appl. Phys. Lett. **84**, 3187 (2004).
[16] S. Cherian, and T. Thundat, Appl. Phys. Lett. **80**, 2219 (2002).
[17] S. Cherian, A. Mehta, and T. Thundat, Langmuir **18**, 6935 (2002).
[18] J. Dorignac, A. Kalinowski, S. Erramilli, and P. Mohanty, Phys. Rev. Lett. **96**, 186105 (2006).
[19] K. S. Hwang, K. Eom, J. H. Lee, D. W. Chun, B. H. Cha, D. S. Yoon, T. S. Kim, and J. H. Park, Appl. Phys. Lett. **89**, 173905 (2006).
[20] G. Y. Chen, T. Thundat, E. A. Wachter, and R. J. Warmack, J. Appl. Phys. **77**, 3618 (1995).
[21] J. Lagowski, H. C. Gatos, and E. S. Sproles Jr., Appl. Phys. Lett. **26**, 493 (1975).
[22] V. Fiorentini, M. Methfessel, and M. Scheffler, Phys. Rev. Lett. **71**, 1051 (1993).
[23] V. Pini, J. Tamayo, E. Gil-Santos, D. Ramos, P. Kosaka, H. D. Tong, C. van Rijn, and M. Calleja, ACS Nano **5**, 4269 (2011).
[24] A. Husain, J. Hone, H. W. C. Postma, X. M. H. Huang, T. Drake, M. Barbic, A. Scherer, and M. L. Roukes, Appl. Phys. Lett. **83**, 1240 (2003).
[25] M. E. Gurtin, X. Markenscoff, and R. N. Thurston, Appl. Phys. Lett. **29**, 529 (1976).
[26] P. Lu, H. P. Lee, C. Lu, and S. J. O'Shea, Phys. Rev. B **72**, 085405 (2005).
[27] M. J. Lachut and J. E. Sader, Phys. Rev. Lett. **99**, 206102 (2007).
[28] M. J. Lachut and J. E. Sader, Appl. Phys. Lett. **95**, 193505 (2009).
[29] D. W. Dareing and T. Thundat, J. Appl. Phys. **97**, 043526 (2005).
[30] G. F. Wang and X. Q. Feng, Appl. Phys. Lett. **90**, 231904 (2007).
[31] Y. Zhang, Q. Ren, and Y.-P. Zhao, J. Phys. D: Appl. Phys. **37**, 2140 (2004).
[32] A. W. McFarland, M. A. Poggi, M. J. Doyle, L. A. Bottomley, and J. S. Colton, Appl. Phys. Lett. **87**, 053505 (2005).
[33] X. Yi and H. L. Duan, J. Mech. Phys. Solids **57**, 1254 (2009).
[34] H. Duan, Acta Mechanica Solida Sinica **23**, 1 (2010).
[35] J. E. Sader, J. Appl. Phys. **89**, 2911 (2001).
[36] J. E. Sader, J. Appl. Phys. **91**, 9354 (2002).
[37] K. Dahmen, S. Lehwald, and H. Ibach, Surf. Sci. **446**, 161 (2000).
[38] K. Dahmen, H. Ibach, and D. Sander, J. Magn. Magn. Mater. **74**, 231 (2001).
[39] M. E. Gurtin and A. I. Murdoch, Arch. Ration. Mech. Anal. **57**, 291 (1974).
[40] S. C. Masmanidis, R. B. Karabalin, I. De Vlaminck, G. Borghs, M. R. Freeman, and M. L. Roukes, Science **317**, 780 (2007).
[41] P. Müller and R. Kern, Surf. Sci. **301**, 386 (1994).
[42] E. H. Mansfield, *The Bending and Stretching of Plates* (Pergamon, New York, 1964).
[43] S. P. Timoshenko and J. N. Goodier, *Theory of Elasticity* (McGraw-Hill, New York, 1951).
[44] S. S. Rao, *Vibration of Continous Systems* (John Wiley & Sons, New Jersey, 2007).
[45] S. P. Timoshenko and S. Woinowsky-Krieger, *Theory of Plates and Shells* (McGraw-Hill, New York, 1959).
[46] L. D. Landau and E. M. Lifshitz, *Theory of Elasticity* (Pergamon, Oxford, 1959).
[47] LUSAS is a trademark of and is available from FEA Ltd. Forge House, 66 High St., Kingston Upon Thames, Surrey KT1 1HN, UK. 3D quadrilateral elements were used. Mesh was refined to 98% convergence.
[48] R. Maranganti and P. Sharma, Phys. Rev. Lett. **98**, 195504 (2007).
[49] D. B. Zhang, E. Akatyeva, and T. Dumitrică, Phys. Rev. Lett. **106**, 255503 (2011).